

Optimized mixing in microfluidic channels

T. Liang¹ and M. West^{2*}

¹*Aeronautics and Astronautics, Stanford University, Stanford, CA 94305, USA*

²*Mechanical Science and Engineering, University of Illinois at Urbana-Champaign, Urbana, IL 61801, USA*

SUMMARY

We develop a topology optimization method for optimizing the shape of pressure-driven microfluidic channels to maximize the passive mixing rate of advected tracers. The optimization procedure uses a relaxation of Stokes flow by allowing a permeable structure and the objective can be a function of either the fluid velocity field or the particle map from inlet to outlet. We present two new channel designs, one that is an optimized version of the herringbone mixer of Stroock et al., and one that mixes more quickly by using a fully 3D structure in the channel. These channels deliver approximately 30% and 60% reductions, respectively, in the 90% mixing lengths. To compare our numerical simulations to experiments, we approximate the inlet-outlet particle map by a Markov Chain and show that this cheaply approximates the true stochastic map. Copyright © 2011 John Wiley & Sons, Ltd.

Received ...

KEY WORDS: Topology optimization; Microfluidic mixing; Chaotic mixing

1. INTRODUCTION

Microfluidic mixing channels. Microfluidic systems control and manipulate liquids in microliter or nanoliter amounts. The study of microfluidics emerged in the 1990s and is now widely applied in various fields such as the development of DNA chips [1], molecular biology [2], chemical reactions [3], transfers of small volumes of materials [4], and lab-on-a-chip technology [5, 6]. One of the challenges in microfluidics is the design of mixing channels, whose objective is to thoroughly mix two or more different liquids. Although the mixers designed by using active components like micro-pumps to stir the flow have very promising results [7, 8], passive mixing devices have advantages in manufacturing simplicity and price.

In this paper, we focus on the design and optimization of passive microfluidic mixing channels. A microfluidic mixing channel typically has cross-section dimension $\ell \sim 100\mu\text{m}$, and Reynolds number $\text{Re} = U\ell/\nu$ is less than 100 [9] (U is the average velocity of the liquid and ν is the kinematic viscosity of the fluid). Fluid flow on this scale is highly laminar and the mixing of materials between streams is purely diffusive. The dimensionless number that controls the length of the channel

*Correspondence to: Email: mwest@illinois.edu

required for mixing is the Péclet number ($Pe = U\ell/D$, where D is the molecular diffusivity). For a pressure-driven mixing channel, the mixing length can be expected to grow linearly with Pe and is usually much more than 1 cm. Hence various designs have been proposed to stir the flow inside the channel and produce transverse velocities to enhance the mixing [9, 10, 11].

The mixing problem has been linked to chaotic mixing protocols, which are believed to have the best mixing results due to the stretching and folding features of chaotic maps. A typical way to realize chaotic mixing is through the design of linked twist maps [11]. However, there is no direct way to realize the designed linked twist map in a mixing channel, either by passive structures or active mechanisms such as variable-frequency pumps or internal moving components. In this paper, we use the techniques developed in topology optimization to find the internal structure of a mixing channel to realize a desired flow field or flow map. The results can be applied to mixing channel design when the desired mixing protocol is known.

Topology optimization. A typical topology optimization problem is to distribute a given amount of material in a design domain, subject to load and support conditions, such that the stiffness of the structure is maximized [12]. The design parameters are usually the spatial distribution of the material. Even though the optimal solution is in general quite sparse in space, the number of variables is often inevitably large in the formulation. Some problems, such as truss topology design, can be formulated as convex optimization problems [13] by relaxing the material density to be variable, and are thus solvable by efficient algorithms. The optimal solution of the relaxed optimization is shown to be a black/white solution and thus also the optimal solution of the original problem. In other cases when the problem has no convex formulation, nonlinear optimization techniques need to be applied and it is in general hard.

Topology optimization has been applied to the design of optimal shapes of pipes or diffusers such that the total potential power drop is minimized [14, 15]. In that work, Darcy flow is used to simulate the flow inside porous material and form a relaxation. The design parameters in this formulation are the permeability of the material on a spatial grid. In this case, the relaxed problem is still non-convex, but can be solved by means of sequential separable and convex programming. A two-step solution procedure is thus applied to find a black/white solution with permeability either 0 or infinity at a point.

In this paper we use the same relaxation strategy [14, 15] to formulate the mixing channel design as a topology optimization problem. We assume that our mixing channel is a periodic repetition of a basic block, which is what we optimize. We use a proxy objective function that is a function of the velocity field or a map between the inlet and the outlet of one period of the channel. These proxy cost functions are chosen so that optimizing them produces the desired mixing or other flow behavior. This results in a nonlinear optimization problem and a sub-gradient method is developed to find the local minimum of the objective function. We do not consider the fabrication issue explicitly when solving the topology optimization problem.

The simulation of advection-diffusion equations. Another challenge in the design of microfluidic mixing channels is that there is no clear measure of how well a channel mixes. In experiments it is common to measure the variance of colored liquids on the cross-section of the channel to see how well they are mixed [9]. However, when doing simulation, this corresponds to

solving the advection-diffusion equation for a 3D flow field in a very long channel with very small diffusion, which is extremely expensive. The problem is that the relationship between the channel structure and the resulting variance of the liquid on a cross-section is very complicated.

In this paper, we develop a Markov Chain model to approximate the mixing process from one channel cross-section to the next, using a high resolution 2D grid. Similar approaches can be found in, for example, [16, 17, 18, 19, 20]. This is a cheap way to replace the solution of the advection-diffusion equation and can let one observe the mixing process and measure the variance of the colored field easily. This model does not represent a high-fidelity solution of the advection-diffusion equation, but it captures the most important factors of the chaotic mixing: stretching, folding and molecular diffusion. In addition, because we can use a high resolution 2D grid, we can keep numerical diffusivity below the physical diffusivity.

Outline of the paper. In Section 2 we describe the mathematical model of mixing channels and how to form the topology optimization problem using a relaxation of Stokes flow to Darcy flow. Section 3 discusses the simulation issue and a Markov chain model is proposed to approximate the solution of the advection-diffusion equation to evolve the color intensity field. Results are given in Section 4 and finally conclusions are in Section 5.

2. FORMING THE OPTIMIZATION PROBLEM

2.1. Mathematical model of a periodic microfluidic mixing channel

We are concerned with mixing in a long and thin channel. Fluids with two different colors (represented by intensities 1 and 0) are injected in one end of the channel and flow through it, driven by body force only. The channel has some internal structure that acts to stir the fluid passively. This structure is periodic with period ℓ_x and the cross-section of the channel has dimension ℓ_y by ℓ_z . The channel is assumed to be long enough so that the velocity field inside is fully developed and hence also periodic with period ℓ_x . Because of the periodic velocity field, we need to solve it for only one period, and we can then use this velocity field to transport the fluid with different colors iteratively to observe the mixing process. In fact, we calculate the streamlines that connect the two ends ($x = 0$ and $x = \ell_x$) of one period length channel and define a Poincaré map. Applying this map repeatedly tells us how a particle moves between different cross-sections along the channel.

As mentioned in the introduction, flow on the microfluidic scale has $Re \sim 1$ and is thus highly laminar. A Stokes partial differential equation is generally a reasonable model of the motion. We simulate the flow by the generalized Stokes equation for incompressible flow:

$$(-\nu\Delta + \alpha)u + \nabla p = b, \quad (1a)$$

$$\operatorname{div} u = 0, \quad (1b)$$

where $u(\mathbf{x})$ and $p(\mathbf{x})$, which are both functions of position $\mathbf{x} = (x, y, z)$, stand for the velocity and pressure fields and b is the body force that drives the flow. It has an elliptic operator $-\nu\Delta + \alpha$ in which ν is the kinematic viscosity and $\alpha(\mathbf{x})$ represents the inverse permeability at \mathbf{x} . When $\alpha(\mathbf{x}) = 0$ it is just Stokes flow with viscosity ν and when $\nu = 0$, one obtains the Darcy equation,

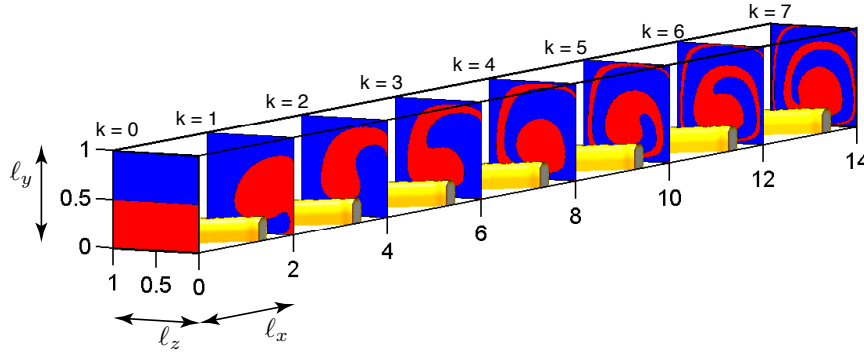


Figure 1. The mixing channel. Liquids with two different colors are originally separate and injected from one end of the channel. The channel consists of repeats of a periodic block of size $\ell_x \times \ell_y \times \ell_z$ containing structures to alter the flow and produce mixing of the colored liquids. In this figure, cross-sections of the color distribution are plotted every period of the structure ($k = 0$ to $k = 7$).

which governs the flow in porous material with permeability α^{-1} . This represents a relaxation of the true problem [14, 15], which is presumed to use impermeable material with $\alpha = \infty$. As we will discuss in Section 4.1, in practice we find that optimal designed typically have α either very low or very high, which we then take to be zero or infinite, respectively.

The liquids to be mixed are assumed to have the same density and viscosity, which is true for many applications when the liquids are solvents carrying different reactants. This assumption is critical for our periodic setting to work, because now we can separate the color intensity field from the velocity field: the velocity field is stationary and periodic but the color intensity field is not. This allows us to use one period of velocity field repeatedly to carry the color intensity and observe the mixing process.

We use a finite-difference method with staggered regular meshes to solve the above equation. Assuming the finite-dimensional approximation of the Laplace, gradient and divergence operators on the given mesh are L , G , and D , the generalized Stokes equation can be represented by

$$\begin{bmatrix} -\nu L + \text{diag}(\bar{\alpha})H & G \\ D & 0 \end{bmatrix} \begin{bmatrix} \bar{u} \\ \bar{p} \end{bmatrix} = \begin{bmatrix} \bar{b} \\ \mathbf{0} \end{bmatrix}, \quad (2)$$

where \bar{u} , \bar{p} , $\bar{\alpha}$, and \bar{b} are vectors, representing finite-dimensional approximations of u , p , α and b , respectively. The linear operator H maps the design parameters $\bar{\alpha}$ to the directional \bar{u} grids.

Let the number of grid cells in the x , y , and z directions be n_x , n_y , and n_z . We define $n_{\bar{u}} = 3n_x n_y n_z$, which is roughly the size of \bar{u} , and $n_{\bar{\alpha}} = n_{\bar{p}} = n_x n_y n_z$, which is roughly the size of $\bar{\alpha}$ and \bar{p} (boundary conditions make these expressions only approximate). A typical case in our examples is $n_x = 144$, $n_y = 24$, and $n_z = 48$.

2.2. Topology optimization

We would like to optimize some objective function $g(\bar{u}, \bar{p}, \bar{\alpha})$ over parameters $\bar{\alpha}$. The direct approach would be to define an optimization problem

$$\text{minimize } g(\bar{u}, \bar{p}, \bar{\alpha}) \quad (3a)$$

$$\text{subject to } \begin{bmatrix} -\nu L + \text{diag}(\bar{\alpha})H & G \\ D & 0 \end{bmatrix} \begin{bmatrix} \bar{u} \\ \bar{p} \end{bmatrix} = \begin{bmatrix} \bar{b} \\ 0 \end{bmatrix}, \quad (3b)$$

$$0 \leq \bar{\alpha} \leq \alpha_{\max}, \quad (3c)$$

where $\alpha_{\max} \in \mathbb{R}$ is a large number to approximate the minimum permeability when α goes to infinity and the structure is solid. The optimization problem has variables \bar{u} , \bar{p} , and α_{\max} , and a large set of nonlinear equality constraints that make the problem extremely hard to solve.

For a given $\bar{\alpha}$, we can solve (3b) to obtain \bar{u} and \bar{p} and there are no inequality constraints on these two variables. We can thus rewrite the optimization and lump the equality constraints into the objective function:

$$\text{minimize } g(\bar{u}(\bar{\alpha}), \bar{p}(\bar{\alpha}), \bar{\alpha}) \quad (4a)$$

$$\text{subject to } 0 \leq \bar{\alpha} \leq \alpha_{\max}. \quad (4b)$$

This formulation reduces the number of variables and eliminates the nonlinear equalities, but it is now harder to evaluate the gradient of the objective function, which we desire for efficiency in the optimization algorithm. We will show later that an adjoint method can be applied to efficiently compute the gradient.

2.3. Objective functions and a descent direction

Objective functions. Our goal is to optimize the shape of the structure inside the channel. That is, to find a vector $\bar{\alpha}$ such that the function $g(\bar{u}, \bar{p}, \bar{\alpha})$ is locally minimized. The ideal objective function is mixing length [9]: the channel length required for the standard deviation of the color intensity on the cross-section to drop by a given ratio. Unfortunately, this is a very complicated function of the channel structure and there is no clear way to find a descent direction to improve it. Hence, we use several steps of heuristic designs to reduce the mixing length.

Two types of objective function will be considered in our formulation. The first one is a function of the velocity field, which is a very direct way to design the flow. In fact, for most applications, a linear function is sufficient:

$$g_1(\bar{u}, \bar{p}, \bar{\alpha}) = \bar{c}^T \bar{u}, \quad (5)$$

for a given vector \bar{c} .

The second type of objective function measures the difference between two maps. For a given velocity field u , the streamlines can be calculated by numerical integration. Each of the streamlines connects a point on the y - z plane at $x = 0$ to another point at $x = \ell_x$. The streamlines thus define an end-to-end flow map $S_u : [0, \ell_y] \times [0, \ell_z] \rightarrow [0, \ell_y] \times [0, \ell_z]$. Define $g_2(u, p, \alpha; S^*) = \|S^* - S_u\|$,

where $S^* : [0, \ell_y] \times [0, \ell_z] \rightarrow [0, \ell_y] \times [0, \ell_z]$ is the desired end-to-end flow map and $\|\cdot\|$ is a norm on scalar maps (which could be relaxed to a distance function). Suppose we know the desired map S^* . The second type of objective function can then be applied to minimize the difference between the current map and the desired map. However, because each streamline needs to be calculated numerically, to define a map would be extremely hard. Therefore we simplify this objective function and let it measure the difference between a set of sample points on the y - z plane. Let (\bar{y}_0, \bar{z}_0) be a set of sample points on the y - z plane at $x = 0$. We have

$$\begin{aligned}(\bar{y}_e^*, \bar{z}_e^*) &= S^*(\bar{y}_0, \bar{z}_0), \\(\bar{y}_e, \bar{z}_e) &= S_u(\bar{y}_0, \bar{z}_0).\end{aligned}$$

We simply define g_2 as

$$g_2(u, p, \alpha; S^*, \bar{y}_0, \bar{z}_0) = \|\bar{y}_e^* - \bar{y}_e\|^2 + \|\bar{z}_e^* - \bar{z}_e\|^2, \quad (6)$$

where $\|\cdot\|$ is the 2-norm of a vector. The above function is a rough measure of how close the maps S_u and S^* are. In our examples, (\bar{y}_0, \bar{z}_0) is chosen as a regular grid of points in the y - z plane.

Adjoint method for $dg_1/d\bar{\alpha}$. To find a descent direction of g_1 with respect to $\bar{\alpha}$, the adjoint method [21] is applied. Let $\bar{v} = [\bar{u}^T \ \bar{p}^T]^T$. The variables \bar{v} and $\bar{\alpha}$ satisfy a set of constraints $R(\bar{v}, \bar{\alpha}) = 0$ defined by (2). If we directly differentiate (4a) with respect to $\bar{\alpha}$ using the chain rule, then it will be necessary to compute $d\bar{v}/d\bar{\alpha}$. Unfortunately, $d\bar{v}/d\bar{\alpha}$ has size $(n_{\bar{u}} + n_{\bar{p}}) \times n_{\bar{\alpha}}$ (very large) and is dense. We would like to calculate $dg_1/d\bar{\alpha}$ without explicitly forming $d\bar{v}/d\bar{\alpha}$. The adjoint method [22] is designed for this situation. We begin with the total derivative of g_1 and R with respect to α :

$$\begin{aligned}\frac{dg_1}{d\bar{\alpha}} &= \frac{\partial g_1}{\partial \bar{\alpha}} + \frac{\partial g_1}{\partial \bar{v}} \frac{d\bar{v}}{d\bar{\alpha}}, \\ \frac{dR}{d\bar{\alpha}} &= \frac{\partial R}{\partial \bar{\alpha}} + \frac{\partial R}{\partial \bar{v}} \frac{d\bar{v}}{d\bar{\alpha}} = 0.\end{aligned}$$

From the second equation, we have

$$\frac{d\bar{v}}{d\bar{\alpha}} = - \left(\frac{\partial R}{\partial \bar{v}} \right)^{-1} \frac{\partial R}{\partial \bar{\alpha}}.$$

Substituting this into the first equation gives:

$$\frac{dg_1}{d\bar{\alpha}} = \frac{\partial g_1}{\partial \bar{\alpha}} - \frac{\partial g_1}{\partial \bar{v}} \left(\frac{\partial R}{\partial \bar{v}} \right)^{-1} \frac{\partial R}{\partial \bar{\alpha}}.$$

Let $\Phi = - \frac{\partial g_1}{\partial \bar{v}} \left(\frac{\partial R}{\partial \bar{v}} \right)^{-1}$. Then Φ satisfies

$$\Phi \frac{\partial R}{\partial \bar{v}} = - \frac{\partial g_1}{\partial \bar{v}}. \quad (7)$$

The above equation is called the adjoint equation. More explicitly, the adjoint equation in our formulation is

$$\begin{bmatrix} -\nu L + \text{diag}(\bar{\alpha})H & G \\ D & 0 \end{bmatrix}^T \Phi^T = \begin{bmatrix} -(\frac{\partial g_1}{\partial \bar{u}})^T \\ 0 \end{bmatrix}. \quad (8)$$

After solving for Φ , we can then evaluate $dg_1/d\bar{\alpha}$ by

$$\frac{dg_1}{d\bar{\alpha}} = \frac{\partial g_1}{\partial \bar{\alpha}} + \Phi \frac{\partial R}{\partial \bar{\alpha}}. \quad (9)$$

In our problem, g_1 does not depend on $\bar{\alpha}$ explicitly, so the first term in the right-hand side of (9) is zero. To solve the adjoint equation (8), we need $\partial g_1/\partial \bar{u}$, which is just \bar{c}^T for g_1 . Note that solving (8) and evaluating (9) have a similar cost to solving (2), which is dramatically less than the cost of forming $d\bar{v}/d\bar{\alpha}$.

Streamlines and $\partial g_2/\partial \bar{u}$. To find $dg_2/d\bar{\alpha}$, the above approach is still valid but we need to form $\partial g_2/\partial \bar{u}$ first. Let the solution of (2) be the discrete velocity field $\bar{u} = [\bar{u}_x^T \ \bar{u}_y^T \ \bar{u}_z^T]^T$. The velocity at any point can be evaluated by linear interpolation. Given an initial point $(0, y_0, z_0)$, a second-order Runge-Kutta method is applied to find the streamline passing through it. Because both the interpolation and Runge-Kutta method have linear weights on \bar{u} , we can write down the following relations:

$$\begin{aligned} x_e &= k_x^T \bar{u}_x + 0, \\ y_e &= k_y^T \bar{u}_y + y_0, \\ z_e &= k_z^T \bar{u}_z + z_0, \end{aligned}$$

where k_x , k_y and k_z are the constant weighting vectors generated by the numerical integration. We set (x_e, y_e, z_e) to be the point that $(0, y_0, z_0)$ is transported to, assuming $x_e = \ell_x$. Then $dy_e/d\bar{u}$ and $dz_e/d\bar{u}$ can be written as

$$\begin{aligned} \frac{dy_e}{d\bar{u}} &= \left[\frac{\partial y_e}{\partial x_e} \frac{dx_e}{d\bar{u}_x}, \frac{dy_e}{d\bar{u}_y}, \mathbf{0}^T \right] = \left[\frac{u_y(\mathbf{x}_e)}{u_x(\mathbf{x}_e)} k_x^T, k_y^T, \mathbf{0}^T \right], \\ \frac{dz_e}{d\bar{u}} &= \left[\frac{\partial z_e}{\partial x_e} \frac{dx_e}{d\bar{u}_x}, \mathbf{0}^T, \frac{dz_e}{d\bar{u}_z} \right] = \left[\frac{u_z(\mathbf{x}_e)}{u_x(\mathbf{x}_e)} k_x^T, \mathbf{0}^T, k_z^T \right], \end{aligned} \quad (10)$$

where $\mathbf{x}_e = (x_e, y_e, z_e)$ and $u_x(\mathbf{x}_e)$, $u_y(\mathbf{x}_e)$ and $u_z(\mathbf{x}_e)$ can also be evaluated by interpolation. Hence $dg_2/d\bar{u}$, where g_2 has the form of equation (6), can be written as

$$\frac{\partial g_2}{\partial \bar{u}} = \sum_{y_e} \frac{\partial g_2}{\partial y_e} \frac{dy_e}{d\bar{u}} + \sum_{z_e} \frac{\partial g_2}{\partial z_e} \frac{dz_e}{d\bar{u}}. \quad (11)$$

2.4. The gradient-based optimization method

We use a gradient-based method to solve (4):

Topology Optimization Algorithm

given a starting vector $\bar{\alpha}^0$
iteration number $i = 0$
cost function $g = g_1$ or g_2
a gradient step scale δ

repeat 1. solve (2) for the velocity field \bar{u} and pressure field \bar{p}
2. solve the adjoint equation (8) and find $\frac{dg}{d\bar{\alpha}}$
3. $\bar{\alpha}^{i+1} = \bar{\alpha}^i - \delta \frac{dg}{d\bar{\alpha}}$
4. project the components of $\bar{\alpha}^{i+1}$ outside $[0, \alpha_{\max}]$ to 0 and α_{\max}
5. $i = i + 1$

until stopping criterion is satisfied

For all of our examples, we use $\bar{\alpha}^0 = \mathbf{0}$ as the initial material distribution, and we do not impose a total material constraint. In step 4 of the algorithm, the clipping of $\bar{\alpha}$ to zero is necessary because material with negative inverse permeability does not make physical sense.

In our formulation, to evaluate the objective function is very expensive, so there is no line search in this algorithm. A fixed step size is used, and the step size is tuned by hand in our examples. The stopping criterion we use is

$$\left\| \frac{\bar{\alpha}^i}{\|\bar{\alpha}^i\|_2} - \frac{\bar{\alpha}^{i+1}}{\|\bar{\alpha}^{i+1}\|_2} \right\|_2 < \epsilon. \quad (12)$$

For all of our examples, we observe that when the structure is formed, the projection of the negative gradient direction gradually aligns with the current $\bar{\alpha}^i$ direction. So the structure shape does not change but the permeability keeps decreasing. Hence this stop criterion performs well in finding the optimal structure shape.

3. SIMULATION OF MIXING IN THE CHANNEL

Consider a channel design consisting of a k repetitions of a channel block of dimensions $\ell_x \times \ell_y \times \ell_z$. We assume, as above, that the flow in the channel is also periodic and satisfies (1). We want to know how separate fluids injected at the channel inlet mix by the time they reach the channel outlet. We let $Y = [0, \ell_y] \times [0, \ell_z]$ the channel cross-section between each channel block and we represent the fluid color on the k th cross-section by a scalar function $f^k : Y \rightarrow \mathbb{R}$, with f taking values from 0 to 1. We will take f^0 to be

$$f^0(y, z) = \begin{cases} 0 & z < \ell_z/2 \\ 1 & z \geq \ell_z/2 \end{cases} \quad (13)$$

and we want to compute the successive color cross-sections f^k , as illustrated in Figure 1. Ideally, we would solve the advection-diffusion equation

$$u \cdot \nabla \phi = D \Delta \phi \quad (14)$$

with appropriate boundary conditions for the scalar color $\phi(\mathbf{x})$, so that $f^k(y, z) = \phi(k\ell_x, y, z)$ for each k . Solving (14) is significantly more expensive than solving for the periodic flow field, as the flow field is only solved on a domain of size $\ell_x \times \ell_y \times \ell_z$, while ϕ is not periodic and so (14) would need to be solved on a domain of size $(k\ell_x) \times \ell_y \times \ell_z$ for k up to $k = 300$ or more. In addition, a very fine grid would be needed to solve (14) to avoid having the numerical diffusion from the discretization dominate the physical diffusion.

Instead of solving (14), we approximate the solution by constructing the particle advection map $S : Y \rightarrow Y$ for a single channel period, and a diffusion operator $\Psi_D(f)$ corresponding to convolution with a Gaussian to give the diffusion of f with diffusivity D . Then we approximate the evolution of f^k by

$$f^{k+1} = \Psi_D(f^k \circ S^{-1}). \quad (15)$$

This approximation lumps the diffusion into the end of each channel periodic block and assumes that all streamlines experience the same diffusion. In reality, streamlines with lower velocities will have longer transport times, so will experience higher diffusion. We do not account for this effect in our approximation, as variations in advection dominate variations in diffusion for spatially variable mixing rates.

This approximation is both much cheaper than solving (14), and also more accurate for any feasible grid resolutions. This is because we only need to discretize the channel cross-sections to compute (15), so we can use a very high resolution 2D mesh and keep the numerical diffusion well below the physical diffusion. With the 3D advection-diffusion equation (14) this would be infeasible.

3.1. Numerical approximation of advection

To formalize the advection of the color tracer by the fluid flow, we define the function advection operator on Y corresponding to the map S is as follows.

Definition 1 (Koopman operator)

Let $f : Y \rightarrow \mathbb{R}$. The *Koopman operator* U_S associated to S gives $U_S f : Y \rightarrow \mathbb{R}$ defined by

$$U_S f = f \circ S, \quad (16)$$

so $(U_S f)(y, z) = f(S(y, z))$.

The Koopman operator evolves scalar functions on Y . As we see from (15), the advection of f^k downstream to f^{k+1} occurs by the Koopman operator $U_{S^{-1}}$ of S^{-1} . We note that the following conservation holds:

$$\iint_Y f^k(y, z) u_x(y, z) dy dz = \iint_Y (U_{S^{-1}} f^k)(y, z) u_x(y, z) dy dz, \quad (17)$$

where $u_x : Y \rightarrow \mathbb{R}$ is the stationary x -component of velocity on the cross-sections $x = 0, \ell_x, 2\ell_x, \dots$, and this can be shown to be an invariant measure of S . This conservation equation expresses the fact that the total “color” flowing in and out of each period of the channel is constant.

We discretize the cross-section Y into a regular grid with $m = m_y \times m_z$ grid cells a_1, a_2, \dots, a_m of size $h \times h$, so a scalar function f on Y can be approximated by its value $(f_m)_i$ on each grid cell a_i , giving a vector $f_m \in \mathbb{R}^m$.

We find the discrete Koopman operator $U_{S^{-1},m}$ using optimal prediction model reduction [23, 24, 25, 26, 27, 20, 19] (see [28] for an overview in the finite dimensional setting), as described in [29]. The discrete optimal predictor $U_{S^{-1},m}$ for the Koopman operator $U_{S^{-1}}$ can be shown [29] to have matrix form

$$(U_{S^{-1},m})_{ij} = \frac{\int_{S(a_j) \cap a_i} \bar{\omega}(y, z) dy dz}{\int_{a_j} \bar{\omega}(y, z) dy dz}, \quad (18)$$

where $\bar{\omega}$ is the invariant distribution of S given by the x -velocity u_x , normalized to give a probability distribution. We numerically approximate the integrals in (18) with quadrature.

3.2. Numerical approximation of diffusion

We define the physical diffusion map Ψ_D to be the $t = 1$ evolution of the diffusion equation with diffusivity D acting on the initial function. That is, $\Psi_D f = \phi(\cdot, 1)$ where $\phi(x, t)$ solves $\phi_t = D\phi_{xx}$ with $\phi(x, 0) = f(x)$. Equivalently, for our case of $Y = [0, \ell_y] \times [0, \ell_z]$, we can write $f(x)$ and $(\Psi_D f)(x)$ in Fourier sine series of the form

$$f(y, z) = \sum_{p,q=1}^{\infty} A_{p,q} \sin\left(\frac{p\pi y}{\ell_y}\right) \sin\left(\frac{q\pi z}{\ell_z}\right) \quad (19)$$

$$(\Psi_D f)(y, z) = \sum_{p,q=1}^{\infty} w_{p,q} A_{p,q} \sin\left(\frac{p\pi y}{\ell_y}\right) \sin\left(\frac{q\pi z}{\ell_z}\right) \quad (20)$$

$$w_{p,q} = \exp(-4\pi^2(p^2 + q^2)D), \quad (21)$$

where $w_{p,q}$ are the specified weights. We write $\Psi_{D,m}$ for the discrete analogue of this, computed using an FFT, scaling the coefficients by $w_{p,q}$, with a final inverse FFT.

Using the numerical advection $U_{S^{-1},m}$ from the previous section, we can evolve a function f^k by the map S with some small error. This error manifests as numerical diffusion or smoothing with diffusivity of the order $D_{\text{num}} \sim h^2$. To simulate the physical diffusion with diffusivity D accurately, we thus need to ensure that h is small enough that $D_{\text{num}} \ll D$, so that the numerical diffusion is negligible compared to the physical diffusion.

Our final discrete evolution for the discrete color fields on channel cross-sections is thus

$$f_m^{k+1} = \Psi_{D,m} U_{S^{-1},m} f_m^k. \quad (22)$$

As discussed above, this evolution is not an accurate solution of the full advection-diffusion equation (14). However, it does capture the most important factors in chaotic mixing: stretching, folding, and the molecular diffusion. We demonstrate later by examples that this approximation agrees well with experimental results.

4. RESULTS

In this section we consider four different optimized channel designs:

1. An interior structure to produce maximum transverse velocity: discussion in Section 4.1, structure shown in Figure 2, mixing cross-sections shown in Figure 3.
2. A boundary structure to produce fast mixing via alternating vortex pairs (a linked twist map): discussion in Section 4.2, structure shown in Figure 4 left, mixing cross-sections shown in Figure 6.
3. An interior structure to produce fast mixing via alternating vortex pairs (a linked twist map): discussion in Section 4.2, structure shown in Figure 4 right, mixing cross-sections not shown.
4. An interior structure to produce a transport map close to a rigid 45° rotation: discussion in Section 4.3, structure shown in Figure 9, mixing cross-sections shown in Figure 10.

Here an interior structure refers to one which can occupy some part of the interior of the flow channel, while a boundary structure is one that is restricted to lie within some given distance of the channel walls. In all cases the structures were generated as described in Section 2, using the algorithm from Section 2.4.

In all of our simulations, we use kinematic viscosity $\nu = 0.01 \text{ g cm}^{-1} \text{ s}^{-1}$, cross-section dimensions $\ell_y, \ell_z \sim 0.01 \text{ cm}$, and we adjust the body force to make the average x -velocity around 1 cm s^{-1} so that $\text{Re} = U\ell/\nu \approx 1$. The grid size we use to discretize the channel cross-section is $h = 1.25 \times 10^{-5} \text{ cm}$, which corresponds to 8×10^4 grid cells per centimeter and a total of $M = 800 \times 800$ grid cells. The numerical diffusion caused by this discretization is $D_{\text{num}} \sim h^2 = 1.5 \times 10^{-10} \text{ cm}^2$ per period of the channel. A 2D FFT/IFFT scheme is applied to add physical diffusion with diffusivity D at least 10^{-9} cm^2 per period, and hence D_{num} is negligible.

As a guide to the order of the Péclet number Pe , consider $\ell = \ell_y = \ell_z = 0.01 \text{ cm}$, $\ell_x = 0.02 \text{ cm}$, $U = 1 \text{ cm s}^{-1}$, and take diffusivity of 10^{-9} cm^2 per period of the channel. Then $D = 10^{-9} \times U/\ell_x = 5 \times 10^{-8} \text{ cm}^2 \text{ s}^{-1}$, and $\text{Pe} = U\ell/D = 2 \times 10^5$. Note that the mesh we use to solve the velocity fields ($n_x \times n_y \times n_z$) is different from the cross-section meshes $m_y \times m_z$ used to evolve the color fields (the latter is much higher resolution).

4.1. Maximizing the downward velocity at the center of the channel

This design is to demonstrate the use of the objective function of type g_1 (see (5)) and address the porous material regularization that we are using.

The mixing channel has dimension $(\ell_x, \ell_y, \ell_z) = (0.02, 0.01, 0.01) \text{ cm}$ per period, and is discretized into $(n_x, n_y, n_z) = (64, 32, 32)$ grid cells. We set \bar{c} in (5) to maximize the average downward (negative y direction) velocity inside the block $[0, \ell_x] \times [0.3\ell_y, 0.7\ell_y] \times [0.3\ell_z, 0.7\ell_z]$. The optimization ran for 46 iterations and the structure shape was obtained as shown in the right of Figure 2. Seven of the streamlines are plotted as well. From the streamlines, it is easy to see that our objective is achieved. In the left of Figure 2 we plot how $\bar{\alpha}$ grows versus optimization iteration number on a line through the channel. From this plot, we see that material is initially added in the center of the channel, but is then later removed by the algorithm, so the gradient direction does change and we are not solving a trivial problem. Moreover, one can clearly observe that the material gradually forms a black/white solution such that eventually $\bar{\alpha}$ tends to only take the value 0 or α_{max} .

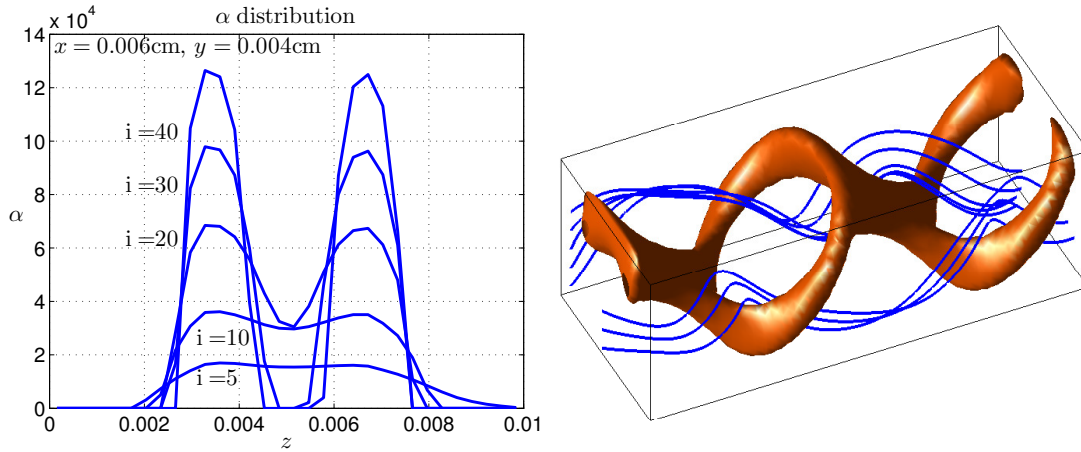


Figure 2. Optimal design for maximum central downward velocity (see Section 4.1). Left: evolution of inverse permeability α versus optimization iteration number i , plotted on a vertical line in the domain. We see that material is initially added in the center of the channel, but is removed in later iterations, showing that the cost function gradient is changing. We also see that the optimal α is tending towards either zero or α_{\max} . Right: the resulting optimal structure after 46 optimization iterations.

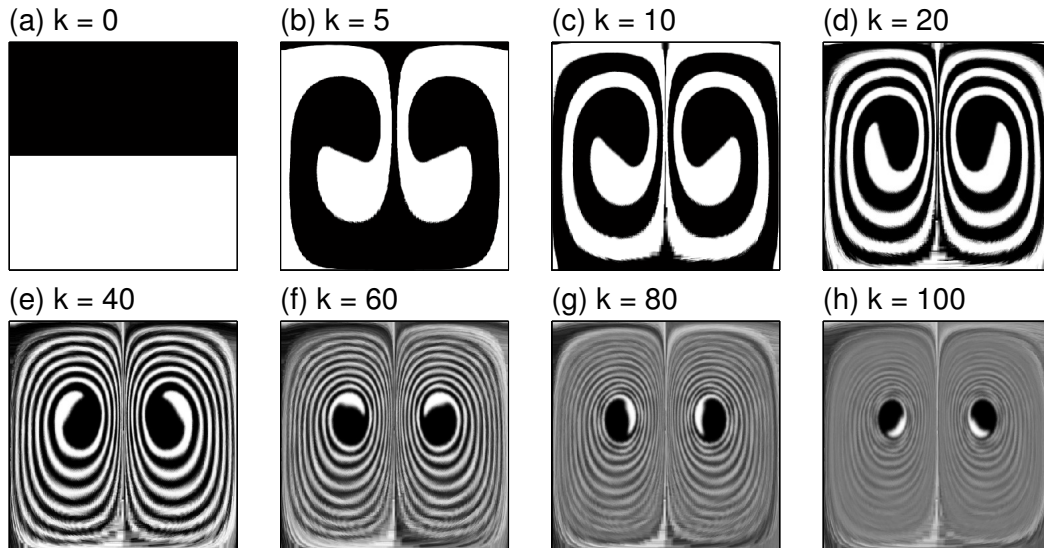


Figure 3. Mixing simulation for the maximum-downward-velocity design shown in Figure 2 and discussed in Section 4.1. The flow does have a very high downward velocity in the center, as expected.

We used the simulation method discussed in Section 3 to simulate the mixing behavior of this system. The result is shown in Figure 3. The system is clearly maximizing the downward velocity at the center of the channel, as designed, which does mix the fluid, but not as well as the designs discussed in the next section.

4.2. Designing a fast-mixing channel

With this design, we want to show how the use of a g_1 kind of objective function can help us to design a mixing channel to realize fast and chaotic mixing. Stroock, et al. [9] proposed a staggered herringbone mixer composed of two sequential regions of ridges; the direction of asymmetry of the

herringbones switches with respect to the center-line of the channel from one region to the next. The herringbone structure is fabricated with two steps of photolithography and is located on the floor of the poly channel. Experiments show that the length of the channel required for mixing grows only logarithmically with Pe , instead of linearly as in a smooth channel. The goal of the herringbone structure is to produce transverse flows for which we can further optimize by the g_1 objective function.

The mixing channel has dimension $(\ell_x, \ell_y, \ell_z) = (0.06, 0.01, 0.02)$ cm per period and is discretized into $(n_x, n_y, n_z) = (144, 24, 48)$ grids. We set c to maximize the downward (negative y direction) velocity inside the offset center block $[0, \ell_x] \times [0, \ell_y] \times [\frac{2}{6}\ell_z, \frac{5}{6}\ell_z]$, which produces one large and one small vortex. We consider two scenarios: (1) the material is restricted to be on the bottom of the channel (the block $[0, \ell_x] \times [0, 0.2\ell_y] \times [0, \ell_z]$) to form a boundary structure, and (2) the material can be put anywhere inside the channel to form an interior structure. The optimal structures of both scenarios, as shown in Figure 4, contain several periods of (almost) the same structure. The same pattern repeats four times in the first case and three times in the second case. One can see that in the first case, the optimal structure is also a herringbone type, but has a higher frequency for the smaller vortex. For the second scenario, the structure is formed by much more material and also tends to have a higher frequency for the smaller vortex.

We emphasize that in both designs the initial structure state was $\bar{\alpha} = 0$, so the formation of the herringbone pattern is entirely driven by the optimization algorithm. Interestingly, it appears to be more efficient to have asymmetric frequencies for the herringbone structure. The choice of domain size that we used for optimization (in particular ℓ_x) does determine the herringbone frequency, as an integer number of structures must fit within this periodic domain.

Just like in the previous example, one can simulate how the channel mixes the colors by the Markov Chain model. However, in order to produce chaotic mixing, the mixer has to be composed of two sequential regions that are symmetric with respect to the plane $z = \frac{1}{2}\ell_z$, and this breaks the periodic boundary condition assumed in obtaining the Markov Chain. In order to perform a correct simulation, we need to solve the flow field for a full cycle of channel.

Let us focus on the first scenario. Since the same structure repeats four times in the solution, we take one of them and call it “L” (with dimension $(\ell_x, \ell_y, \ell_z) = (0.015, 0.01, 0.02)$ cm). The symmetric structure of “L” is thus called “R”. We can build an n -cycle channel by connecting $n/2$ L structures and $n/2$ R structures together. It thus has the period $0.015n$ cm. For fixed $Pe = 1.2 \times 10^4$, we solve the flow field for different n -cycles with $n = 6, 8, 10$ and 12 , and find that when $n = 8$, the channel has the best mixing. Hence in Figure 5, the 8-cycle mixing channel is used to perform the simulation with different Pe . We adjust Pe by changing the FFT/IFFT diffusivity between each 8-cycle (0.12 cm). The trajectories have the same tendency as the experiment results in Figure 3(D) in [9]. We define the mixing length x_{90} as the channel length required for the standard deviation to drop to 0.05 (shown by a dashed line in Figure 5). We see that the mixing length grows linearly with $\log(Pe)$, which matches the experimental results [9].

In Figure 6 we show cross-sectional plots of two of the simulations in Figure 5, where the channel is an 8-cycle and Pe is 1.2×10^6 (left column) and 1.2×10^9 (right column). The first four rows show the cross-sections at the end of the 1st to the 4th cycle, and the last row shows the cross-sections at the end of the 9th cycle. From this comparison we can clearly see how the chaotic mixing protocol enhances mixing even when diffusion is very small.

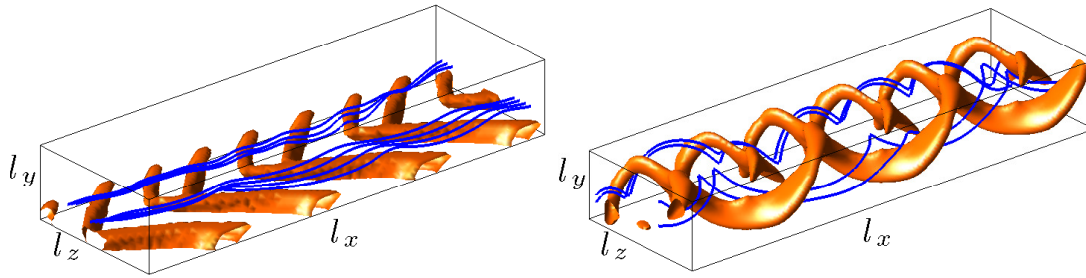


Figure 4. Optimal channel structures for fast mixing (see Section 4.2), with a pair of asymmetric vortices. Left: boundary optimal solution with material restricted to lie only in a region near the boundary. Right: interior optimal solution with no restrictions on material placement.

As for the 3D structure, the best n -cycle we found was $n = 2$ ($\ell_x = 0.04$ cm), because this structure stirs the flow a great deal. To further compare our optimized structures and the design in [9], we also performed a simulation of Stroock's staggered herringbone mixer. The mixing length versus $\log(\text{Pe})$ for the three simulations and the experiment data given in [9] are plotted in Figure 7. We see that our simulation (\times) of Stroock's design has a slightly longer mixing length than the experiment data (\diamond) when Pe is small, and they agree well when $\text{Pe} \approx 10^6$ ($\log(\text{Pe}) = 14$). As for our optimal mixing channel designs (\square for the herringbone, and \circ for the 3D structures), they both significantly outperform Stroock's design in our simulations. To quantify this improvement, consider $\log(\text{Pe}) = 12$, where x_{90} is reduced from 1.5 cm (Stroock's herringbone) to 1.0 cm (optimal herringbone) or 0.6 cm (optimal 3D structure). The optimized channels thus have improvements of 30% and 60%, respectively, in mixing lengths.

We emphasize that we are not directly optimizing the mixing rate of the channel. Instead, only the proxy cost function g_1 is being optimized, to produce higher downward velocities at the offset point in the channel. These results thus indicate that this is a reasonable function to optimize when the goal is fast mixing, as it is producing a channel with a linked-twist-type structure with strong twisting for a short channel length.

In Figure 8(a) and (b) we plot the cross-section at the end of the 5-th cycle of our optimal herringbone solution and Stroock's design, for $\log(\text{Pe}) = 14$. We can compare the simulation in Figure 8(b) with Figure 3(C) in [9] to see how similar they are. This suggests that our approximate Markov Chain mixing model is indeed valid when the diffusion is small.

For the above two cases, the average flow velocity in the x direction is around 1.2 cm s^{-1} . We use the same body force for the simulation of the optimal 3D structure, and adjust the diffusivity to make $\log(\text{Pe}) = 14$. The optimal 3D structure has a much shorter cycle length ($\ell_x = 0.04$ cm). Hence we plot the cross-section of it at the end of 15-th cycle in Figure 8(c). It shows that when $x = 0.6$ cm, the mixing is stronger than either herringbone type channel. However, since there is more material inside the channel, for the same body force, the average flow velocity in the 3D structure channel is only 0.2 cm s^{-1} —six times slower than the herringbone type channels. Hence when we plot the cross-section of this mixing channel at time $t = 0.7 \text{ s}$ in Figure 8(d), it is not significantly better than the other two channels at $t = 0.5 \text{ s}$ and $t = 0.6 \text{ s}$. This means that if we care more about mixing time rather than mixing length, or if the available pressure is limited, then the 3D structure may not be the preferable choice.

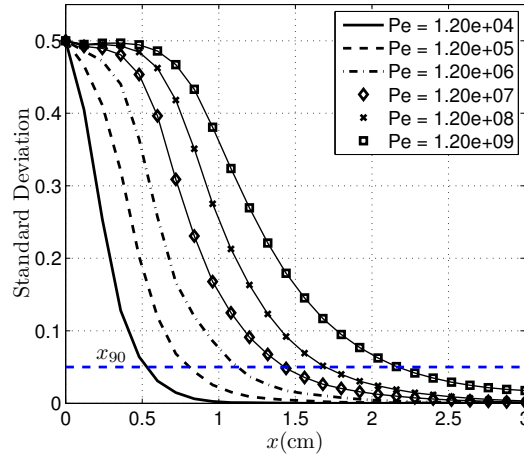


Figure 5. Variation of mixing (standard deviation of color field f) with distance downstream and influence of changing diffusivity D and hence changing Péclet number Pe , for the 8-cycle optimal herringbone structured channel (see Section 4.2 and Figure 4 left).

4.3. Designing a rotation map

The channel designs in previous sections all used linear cost functions g_1 to optimize fluid velocity at certain points in the channel. In this section we demonstrate how the cost function g_2 in (6) can be used to design channel that produces a given transport map S^* , using a test case of a twist map, as would be used to implement a linked twist mixer [11].

There are various kinds of twist maps, for example, $S^* : (y, z) \mapsto (y_e, z_e)$, for

$$\begin{aligned} y_e &= y_c + r \cos(\alpha + \theta), \\ z_e &= z_c + r \sin(\alpha + \theta), \end{aligned}$$

where

$$\begin{aligned} \alpha &= \text{atan2}(y - y_c, z - z_c), \\ r &= \sqrt{(y - y_c)^2 + (z - z_c)^2}. \end{aligned}$$

This defines a twist map centered at (y_c, z_c) with a fixed angle of rotation θ . This is not a realistic map for a channel because it does not satisfy the non-slip boundary conditions on the walls. Nonetheless, we use this as our desired map S^* , with the understanding that our optimized S map will only approximate S^* near the channel center. Again, the mixing channel has dimension $(\ell_x, \ell_y, \ell_z) = (0.02, 0.01, 0.01)$ cm per period, and is discretized into $(n_x, n_y, n_z) = (64, 32, 32)$ grid cells. We use the objective function g_2 from (6) for the above desired map and set $(y_c, z_c) = (0.5\ell_y, 0.5\ell_z)$ and $\theta = 45^\circ$.

The structure after 40 optimization iterations is shown on the left of Figure 9. A set of streamlines starting from 41×41 regular grid points are calculated, and the end points, which form the twisted grid, are plotted on the right of Figure 9 overlaying the original grid. The extra-thick line shows a block whose edges are originally parallel to the channel walls and now rotated almost 45° . In Figure 10 we show the mixing cross-sections of this channel. In the first 7 periods we can see how

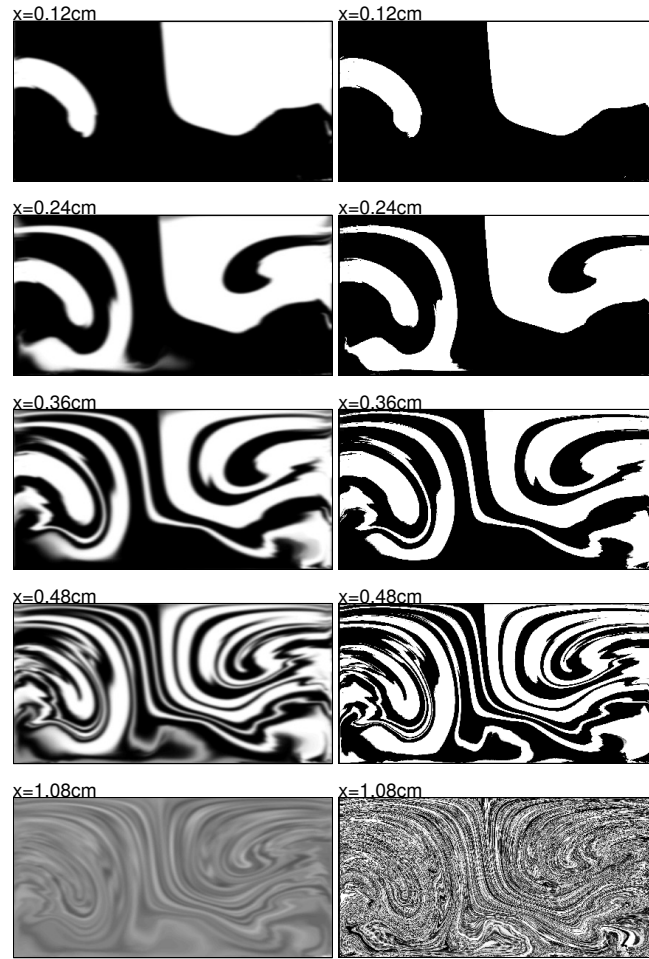


Figure 6. Mixing cross-sections for the 8-cycle optimal herringbone structured channel (see Section 4.2 and Figure 4 left), for $Pe = 1.2 \times 10^6$ (left) and 1.2×10^9 (right). The first four rows show cross-sections after 1 to 4 cycles, while the last row shows cross-sections after , we plot the cross-sections of the end of the 1st to the 4th cycle for both cases. The bottom two plots show the cross-sections of the end of the 9th cycle for both cases. We see that mixing is occurring even with very small diffusivity.

it rotates the boundary between the colored liquids by roughly 45° each period. The last plot in Figure 10 shows the color field at the 100th iteration.

Obviously, this channel does a bad job in mixing, but it is possible that this design route could lead to suitably offset twist maps that could be combined into an efficient mixing channel.

Interestingly, unlike the optimal channel designs found in Sections 4.1 and 4.2, the optimal structure for this design is not solid. That is, the optimal α has values between 0 and α_{\max} . To actually fabricate this structure, a porous material would be needed.

5. CONCLUSION

We have demonstrated a topology optimization method to design the flow field of a periodic microfluidic channel, using the relaxation [14, 15] of Stokes flow in an irregular geometry to

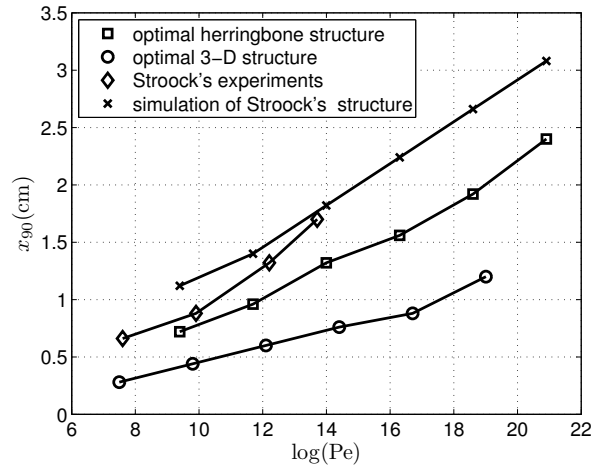


Figure 7. Mixing length x_{90} versus Péclet number for fast-mixing channel designs. We see that our numerical results (\times) agree reasonably well with experiments (\diamond). Comparing numerical simulations, the optimal boundary herringbone structure (\square) is superior to the Stroock structure (\times), while the optimal interior 3D structure (\circ) is the best.

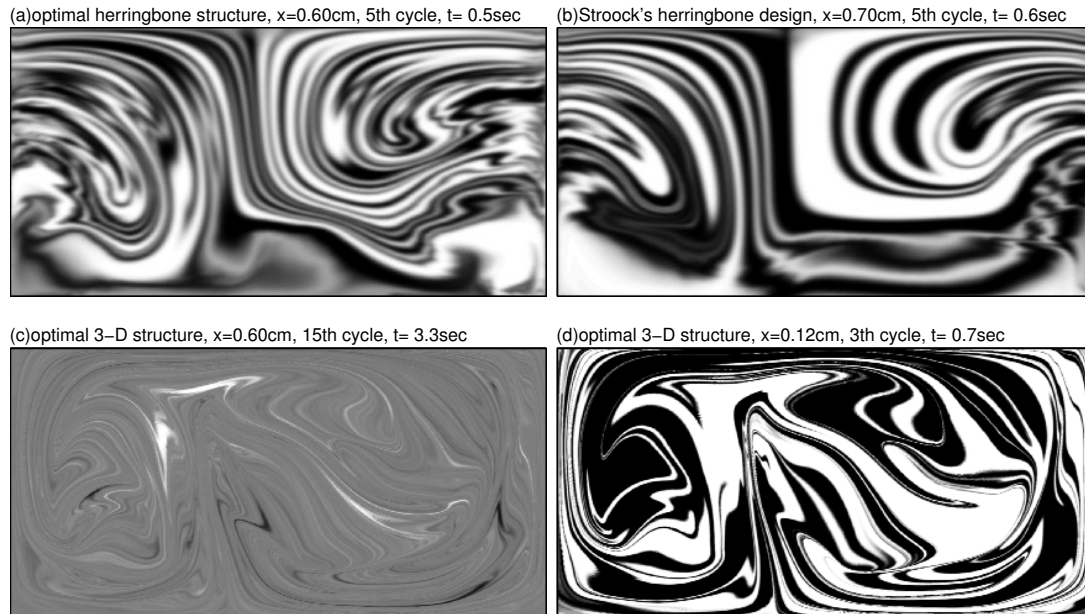


Figure 8. Mixing cross-sections for the fast-mixing designs: (a) the optimal herringbone structure at the end of its 5th cycle; (b) the simulation of Stroock's herringbone design at the end of its 5th cycle; (c) the optimal 3D structure at the end of its 15th cycle; and (d) the optimal 3D structure at the end of its 3th cycle. The color distribution in (b) is almost the same as the experimental result shown in Figure 3(C) in [9], validating the numerical results. Plots (c) and (d) show that although the 3D structure has a much smaller mixing length (x_{90}), it also slows the flow much more. For the same body force, the average velocity in the x -direction is only $1/6$ of that for the herringbone type structures. Hence for the same body force and the same mixing time, the 3D structure is not better than the optimal herringbone structure.

Darcy flow with porous material. The objective function can be either a function of velocity components or a distance between inlet-outlet flow maps, and the optimization uses gradient descent with adjoint method gradient calculation. We also developed a probabilistic model to approximate the solution of the advection-diffusion equation on the cross-sections of the mixing channel. We

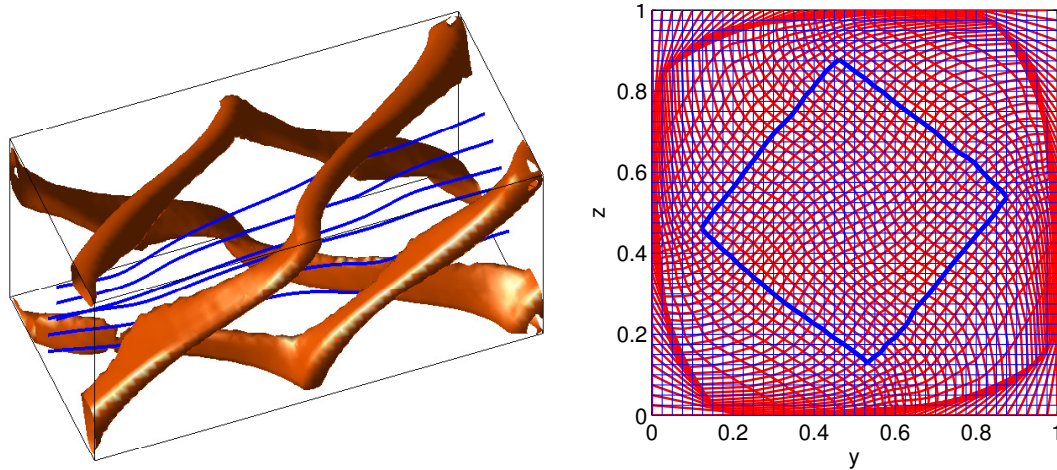


Figure 9. Optimal structure to twist the flow by 45° . Left: structure and streamlines (note that the structure is not solid, but is porous, unlike all other optimal structures in this paper). Right: particle transport map for one period of this structure, with a regular grid and its image overlaid. A thick line shows the image of a square whose edges were originally parallel to the boundary, but is now rotated by 45° as desired. The non-slip boundary conditions means that this map is not a rigid rotation near the boundary.

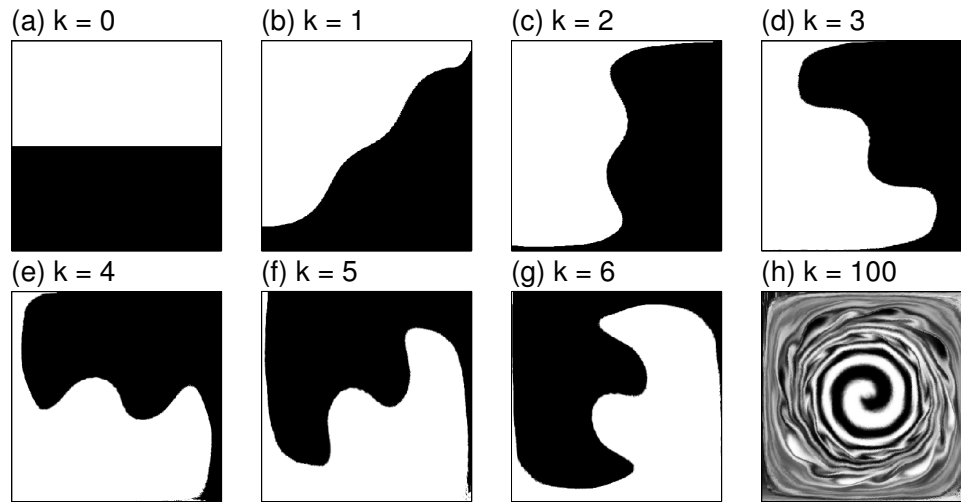


Figure 10. Mixing cross-sections for the rotating channel design shown in Figure 9. For the first 6 periods, the flow field is approximately rotated 45° per period. The last plot shows the cross-section at the 100th iteration.

demonstrated the feasibility of this model by reproducing the experimental results given in [9] with reasonable accuracy. Using our topology optimization method, we presented improved mixing channel designs that reduce the mixing length by 30% (optimal herringbone) and 60% (optimal 3D structure). Of course, these results are only in simulation and may not be reflected by experimental implementations.

Although it may be possible to improve mixing rates by designing flow maps, such as twist maps, it is possible that the resulting channel structures will be porous, as we saw in Section 4.3. Such channels may pose fabrication challenges, making them infeasible in practice.

While we have optimized proxy cost functions, such as downward velocities at certain points, it would be attractive to directly optimize mixing. This could possibly be done by taking the cost

function to be the variance or mix-norm [30] of a color field after a certain channel length, for example, although the efficient computation of gradients could present challenges.

One choice of cost function which might seem appealing, but which we believe does not work in practice, is the second largest eigenvalue modulus (SLEM) [31] of the approximate advection map $U_{S^{-1},n}$. While minimizing the SLEM does maximize the worst-case long-time mixing over all inlet color distributions, we are much more concerned with particular initial conditions (poorly mixed ones) and the initial transient mixing behavior.

In fact, the transient phenomena may be unrelated to the eigenvalues of $U_{S^{-1},n}$, and have nontrivial relation to the pseudospectra [32]. Perhaps the famous examples feature the so-called “cutoff phenomenon” in finite Markov Chains [33, 34, 35], which have interesting connections with chaotic mixing [29, 36].

The mixing behavior of the fast-mixing channels shown in Figure 5 show cutoff-type behavior: as Pe becomes larger, the standard deviation initially stays high for a longer time before dropping rapidly. So even though the mixing length grows logarithmically with Pe , for a fixed Pe we cannot halve the channel length and expect to see half the mixing. Instead, for a given Pe , there is a certain channel length necessary to have reasonable mixing. A too-short channel may produce almost no mixing, while a too-long channel is unnecessary.

Such multi-stage mixing trajectories have been widely observed and studied in chaotic map mixing: see [37, 38, 39, 40, 41] for examples. In [29], the authors study the standard map with small diffusion, and show how the multi-stage mixing behavior of this chaotic map is related to the cutoff phenomenon for Markov chains.

REFERENCES

1. Burns MA, Johnson BN, Brahmamandra SN, Handique K, Webster JR, Krishnan M, Sammarco TS, Man PM, Jones D, Heldsinger D, *et al.*. An integrated nanoliter DNA analysis device. *Science* 1998; **282**(5388):484–487. DOI:10.1126.
2. Beebe DJ, Mensing GA, Walker GM. Physics and applications of microfluidics in biology. *Annual Review of Biomedical Engineering* 2002; **4**:261–286.
3. Andersson H, van der Wijngaart W, Enoksson P, Stemme G. Micromachined flow-through filter-chamber for chemical reactions on beads. *Sensors and Actuators B* 2000; **67**:203–208.
4. Sammarco TS, Burns MA. Thermocapillary pumping of discrete drops in microfabricated analysis devices. *AIChE* 1999; **45**:350–366.
5. Weigl BH, Bardell RL, Cabrera C. Lab-on-a-chip for drug development. *Advanced Drug Delivery Reviews* 2003; **55**(3):349–377.
6. Stone HA, Stroock AD, Ajdari A. Engineering flows in small devices: Microfluidics toward a lab-on-a-chip. *Annual Review of Fluid Mechanics* 2004; **36**:381–411. DOI:10.1146.
7. Yang Z, Goto H, Matsumoto M, Maeda R. Ultrasonic micromixer for microfluidic systems. *The Thirteenth Annual International Conference on Micro Electro Mechanical Systems*, 2000; 80–85.
8. Deshmukh A, Liepmann D. Continuous microfluidic mixing using pulsatile micropumps. *American Physical Society 53rd Annual Meeting of the Division of Fluid Dynamics*, 2000.
9. Stroock AD, Dertinger SKW, Ajdari A, Mezić I, Stone HA, Whitesides GM. Chaotic mixer for microchannels. *Science* 2002; **295**(5555):647–651, doi:10.1126/science.1066238.
10. Ottino JM, Wiggins S. Designing optimal micromixers. *Science* 2004; **305**(5683):485–486, doi: 10.1126/science.1099343.
11. Wiggins S, Ottino JM. Foundations of chaotic mixing. *Philosophical Transactions of the Royal Society A: Mathematical, Physical and Engineering Sciences* 2004; **362**(1818):937–970.

12. Bendsøe MP, Sigmund O. *Topology Optimization: Theory, Methods, and Applications*. Springer: New York, 2003. ISBN 3540429921.
13. Ben-Tal A, Nemirovski A. Robust truss topology design via semidefinite programming. *SIAM Journal on Optimization* 1997; **7**(4):991–1016, doi:http://dx.doi.org/10.1137/S1052623495291951.
14. Evgrafov A. The limits of porous materials in the topology optimization of Stokes flows. *Applied Mathematics and Optimization* 2005; **52**(3):263–277, doi:10.1007/s00245-005-0828-z.
15. Borrvall T, Petersson J. Topology optimization of fluids in Stokes flow. *International Journal for Numerical Methods in Fluids* 2003; **41**(1):77–107, doi:10.1002/d.426.
16. Dellnitz M, Junge O. On the approximation of complicated dynamical behavior. *SIAM Journal on Numerical Analysis* 1999; **36**(2):491–515.
17. Dellnitz M, Junge O. Set oriented numerical methods for dynamical systems. *Handbook of Dynamical Systems II: Towards Applications*. World Scientific Publishing, 2002; 221–264.
18. Froyland G. Approximating physical invariant measures of mixing dynamical systems in higher dimensions. *Nonlinear Analysis, Theory, Methods and Applications* 1998; **32**(7):831–860.
19. Froyland G. Markov modelling for random dynamical systems. *Proceedings of Equadiff 99, Berlin, Germany*, 1999.
20. Froyland G. Extracting dynamical behaviour via Markov models. *Nonlinear Dynamics and Statistics*. Birkhäuser: Basel, 2001; 283–324.
21. Reuther JJ, Jameson A, Alonso JJ, Rimlinger MJ, Saunders D. Constrained multipoint aerodynamic shape optimization using an adjoint formulation and parallel computers, part 1. *Journal of Aircraft* 1999; **36**(1):51–60.
22. Errico RM. What is an adjoint model? *Bulletin of the American Meteorological Society* 1997; **78**:2577–2591.
23. Chorin AJ, Hald OH. *Stochastic Tools in Mathematics and Science*. Springer Science and Business, 2006.
24. Chorin AJ, Kupferman R. Optimal prediction and the Mori-Zwanzig representation of irreversible processes. *Proceedings of the National Academy of Sciences* 2000; **97**:2968–2973.
25. Mori H. Transport, collective motion, and Brownian motion. *Prog. Theor. Phys* 1965; **33**(3):423–455.
26. Zwanzig R. Problems in nonlinear transport theory. *Systems far from equilibrium*, Garrido L (ed.). Springer: Berlin, 1980.
27. Evans D, Morriss G. *Statistical mechanics of nonequilibrium liquids*. Cambridge University Press, 2008.
28. Beck CL, Lall S, Liang T, West M. Model reduction, optimal prediction, and the Mori-Zwanzig representation of Markov chains. *Proceedings of the 48th IEEE Conference on Decision and Control*, 2009; 3282–3287.
29. Liang T, West M. Numerical evidence of cutoffs in chaotic mixing by the standard map 2011. (preprint).
30. Mathew G, Mezić I, Petzold L. A multiscale measure for mixing. *Physica D* 2005; **211**(1-2):23–46.
31. Boyd S, Diaconis P, Xiao L. Fastest mixing Markov Chain on a graph. *SIAM Review* 2004; **46**(4):667–689.
32. Trefethen LN, Embree M. Further examples and applications. *Spectra and Pseudospectra*. Princeton University Press: Princeton, 2005; 508–525.
33. Diaconis P. The cutoff phenomena in finite Markov Chains. *The Proceedings of the National Academy of Sciences*, vol. 93, 1996; 1659–1664.
34. Diaconis P, Saloff-Coste L. Separation cut-offs for death and birth chain. *Annals of Applied Probability* 2006; **16**(4):2098–2122.
35. Saloff-Coste L. Random walks on finite groups. *Probability on Discrete Structures, Encyclopaedia of Mathematical Sciences*, vol. 110. Springer: New York, 2004; 263–346.
36. Liang TC, West M. The cutoff phenomenon and mixing by chaotic maps 2011. (preprint).
37. Thiffeault JL, Childress S. Chaotic mixing in a torus map. *CHAOS* 2003; **13**(2):502–507.
38. Thiffeault JL. Advection-diffusion in Lagrangian coordinates. *Physics Letters A* 2003; **309**(5):415–422.
39. Thiffeault JL. Scalar decay in chaotic mixing. *Transport in Geophysical Flows: Ten Years After, Proceedings of the Grand Combin Summer School*, 2004.
40. Tsang YK, Antonsen TM Jr, Ott E. Exponential decay of chaotically advected passive scalars in the zero diffusivity limit. *Physical Review E* 2005; **71**:066 301.
41. Haynes PH, Vanneste J. What controls the decay of passive scalars in smooth flows? *Physics of Fluids* 2005; **17**:097 103.